

SPARSE RECONSTRUCTION OF SURFACE LOADS ON AIRCRAFT USING POD AND RBFNN

Xuyi Jia¹, Chunlin Gong¹, Chunna Li¹

¹Shaanxi Aerospace Flight Vehicle Design Key Laboratory, School of Astronautics, Northwestern Polytechnical University, Xi'an 710072, China

Abstract

Surface loads based on the measurements from sensors in wind tunnel test or during flight are crucial for aerodynamic design, health monitoring and flight control. However, obtaining the complete surface loads in real-time is challenging due to the limitations of available measurements. To handle this problem, we propose a sparse reconstruction modeling method based on proper orthogonal decomposition (POD) and radial basis function neural network (RBFNN). This method leverages the dimensionality reduction capabilities of POD to extract the dominant modes of surface loads, and then use RBFNN to accurately predict the mode coefficients based on sparse measurements. Furthermore, to improve the accuracy of sparse reconstruction, we have developed an objective function that integrates the surface loads in optimizing the sensor locations. The case study of the *DLR-F6* aircraft shows that a weight of 0.25 for the objective function provides the best reconstruction performance. Additionally, a minimum of 240 modeling samples is required to ensure the accuracy of the sparse reconstruction model. Specifically, with just 37 sensors, we can achieve real-time sparse reconstruction of surface pressure coefficients.

Keywords: Sparse reconstruction; Surface loads; Proper orthogonal decomposition; Sensor locations optimization; Aircraft

1. Introduction

In the aerospace field, sparse reconstruction is widely applied for acquiring aerodynamic loads on aircraft surfaces both in wind tunnel testing and actual flight conditions. [1-3]. And a comprehensive sparse reconstruction process for surface loads includes two main components: constructing the sparse reconstruction model and optimizing sensor locations [4].

The sparse reconstruction model directly affects the efficiency and accuracy of the sparse reconstruction. In general, sparse reconstruction models can be divided into three types: compressed sensing, neural network and surrogate model based on reduced-order model (ROM). Compressed sensing, originally developed as a signal processing theory, reconstructs signals from minimal observations by utilizing their sparse characteristics [5]. This model finds widespread application in fields such image processing, communications, and fluid dynamics. Bai et al. reconstructed particle image velocimetry flow data via compressed sensing [6]; Sha et al. utilized compressed sensing to reconstruct the pressure field of cavitation hydrofoils [7]. However, compressed sensing imposes stringent requirements on data sparsity and involves high computational complexity for reconstructing high-dimensional data. The neural network-based model utilizes intelligent algorithms [8], such as deep neural network, to directly establish a mapping model from sparse measurements to high-

dimensional system data. Santos et al proposed an encoder–decoder architecture and reconstructed nonlinear flow fields using limited sensor measurements [9]. This model demonstrates high reconstruction accuracy, particularly for nonlinear systems. However, training neural networks with complex architectures leads to low problem-solving efficiency, especially when optimizing sensor locations. The surrogate model based on ROM is a composite model that reduces high-dimensional system data to low-dimensional mode coefficients using ROM [10] and establishes a mapping relationship from sparse measurements to mode coefficients using surrogate models with simple architecture. Zhang et al. proposed a sparse reconstruction model based on Dynamic mode decomposition and long short-term memory, enabling the prediction of unsteady flow around a cylinder from sparse sensor measurements [11]. This model effectively tackles the problem of low modeling efficiency and thereby achieving widespread adoption.

In summary, taking into account the accuracy and efficiency of the aforementioned three types of sparse reconstruction models, this paper adopts the surrogate model based on ROM.

The sensor locations are also crucial for the accuracy of sparse reconstruction [12-13], highlighting the need for their optimization. Heuristic optimization algorithms [14] are commonly employed to ensure global optimization. Zhao et al. utilized the particle swarm optimization algorithm to obtain the best sensor locations for sparse reconstruction of airfoil surface pressure [4]. Additionally, genetic algorithm [15], Differential evolution (DE) [16] and NSGA-II [17] have also been successfully applied to sensor location optimization in various sparse reconstruction problems. However, in existing sensor location optimization problems, the objective function typically includes only the system data to be reconstructed, without incorporating additional physical qualities.

Recent data-driven modeling studies indicate that incorporating additional physical quantities as constraints or objective functions can improve the modeling accuracy of the original physical quantities [18-19]. Therefore, in sensor location optimization problem for sparse reconstruction of surface loads, the integral quantities of surface loads can be included in the objective function to enhance reconstruction accuracy.

In this work, we researched the sparse reconstruction of surface aerodynamic loads on aircraft. To ensure modeling efficiency, we constructed a sparse reconstruction model based on proper orthogonal decomposition (POD) and radial basis function neural network (RBFNN). To improve reconstruction accuracy, we devised an enhanced objective function for sensor location optimization by fusing distributed and concentrated forces. The proposed method is applied to the sparse reconstruction of surface pressure coefficients on the *DLR-F6* aircraft.

2. Sparse reconstruction method

The proposed sparse reconstruction method is introduced in this section. Taking the sparse reconstruction of surface pressure coefficients of the aircraft as an example, Figure 1 shows the architecture of the sparse reconstruction method. The whole modeling process consists of two parts: constructing the sparse reconstruction model and optimizing the sensor locations. The purpose of the sparse reconstruction model is to map sparse measurements to surface distributed loads and solve the objective function in sensor locations optimization. Sensor locations optimization aims to provide new sensor locations during optimization, update the sparse reconstruction model, and obtain optimum sensor locations through iterative convergence. The specific processes of the sparse reconstruction model and sensor optimization are outlined below. It is worth noting that both the sparse measurements and the surface pressure coefficients in this work are derived from numerical simulations.

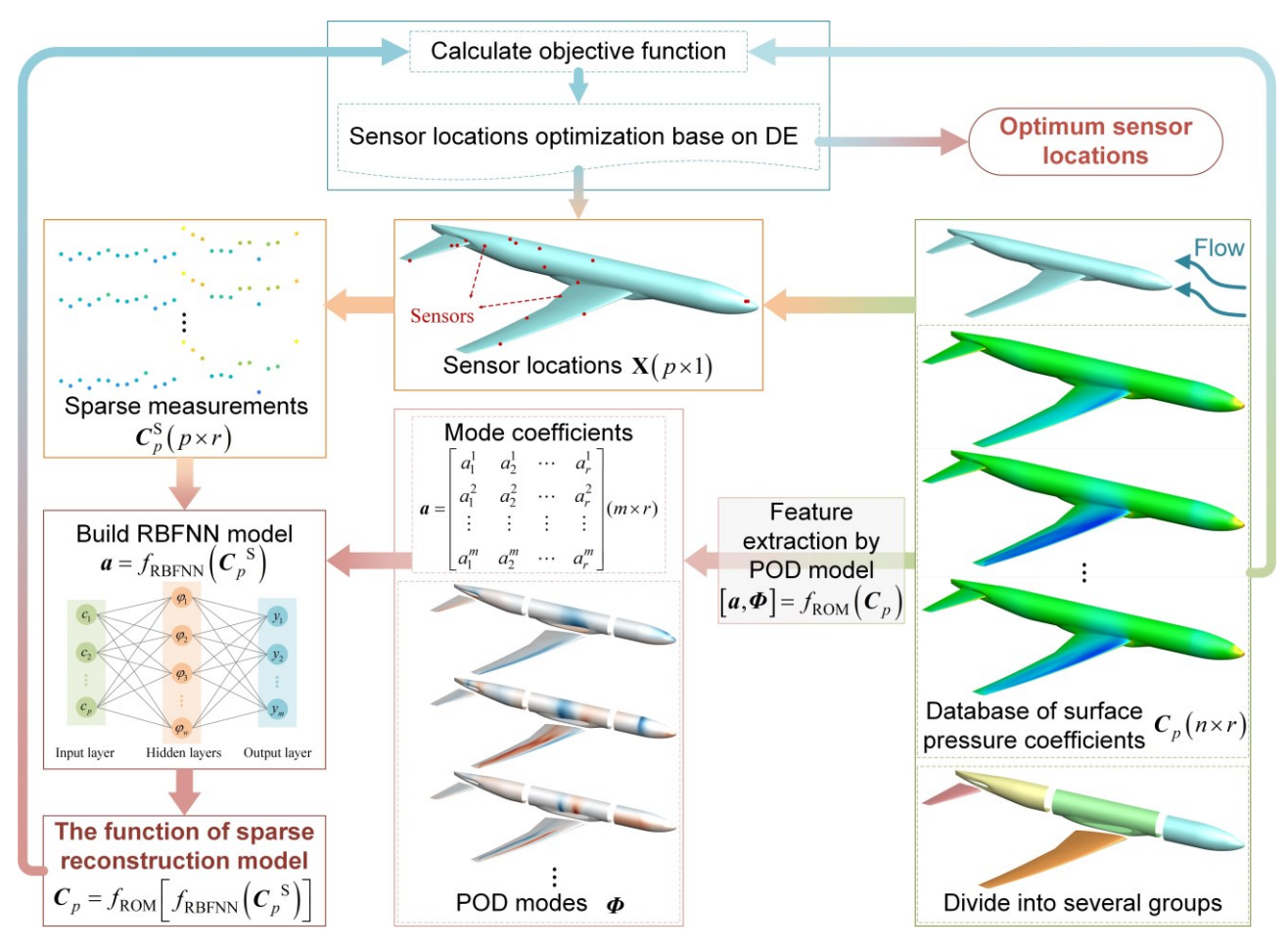


Figure 1 – The architecture of the proposed sparse reconstruction method

2.1 Sparse reconstruction model based on POD and RBFNN

The modeling and reconstructing process of the sparse reconstruction model are shown in Figure 2.

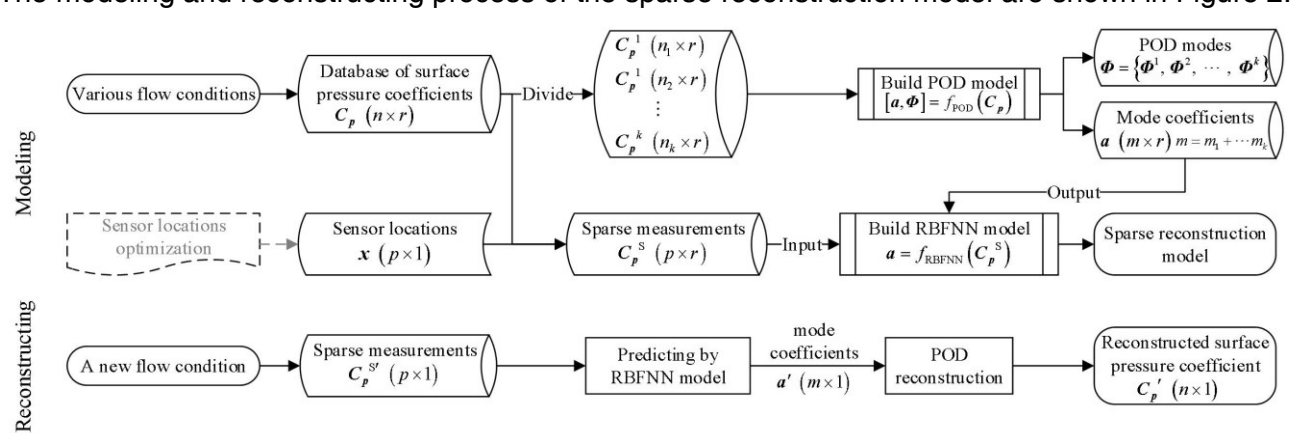


Figure 2 – The schematic diagram of modeling and reconstructing process of the sparse reconstruction model

In the modeling stage, the database of surface pressure coefficients $\boldsymbol{C}_p = \left[\boldsymbol{C}_{p_1}, \boldsymbol{C}_{p_2}, \cdots, \boldsymbol{C}_{p_k}\right]^{\mathrm{T}} \in \mathbb{R}^{n \times r}$ under various flow conditions is first generated through numerical simulation. Divide \boldsymbol{C}_p into several groups based on the components of the aircraft, as shown in equation (1). For each group, the dimension and complexity are less than the whole surface pressure coefficients, which is helpful to improve the modeling accuracy of the ROM [20].

$$\boldsymbol{C}_{p} = \left\{ \boldsymbol{C}_{p}^{1} \in \mathbb{R}^{n_{1} \times r}, \boldsymbol{C}_{p}^{2} \in \mathbb{R}^{n_{2} \times r}, \cdots, \boldsymbol{C}_{p}^{k} \in \mathbb{R}^{n_{k} \times r} \right\} (0 < n_{1}, n_{2}, \cdots, n_{k} < n)$$
 (1)

Where, $0 < n_1, n_2, \dots, n_k < n$ and $n_1 + n_2 + \dots + n_k = n$.

Then, the POD model (as described in section 3.1) for each group is established, thus the modes $\Phi = \{\Phi^1, \Phi^2, \cdots, \Phi^k\}$ and corresponding mode coefficients $a = [a^1, a^2, \cdots, a^k]^T \in \mathbb{R}^{m \times r}$ can be obtained. The built POD models can be expressed by equation (2).

$$\begin{cases}
[\boldsymbol{a}^{1}, \boldsymbol{\Phi}^{1}] = f_{\text{POD}-1}(\boldsymbol{C}_{p}^{1}) & (\boldsymbol{a}^{1} \in \mathbb{R}^{m_{1} \times r}, \boldsymbol{\Phi}^{1} \in \mathbb{R}^{n_{1} \times m_{1}}) \\
[\boldsymbol{a}^{2}, \boldsymbol{\Phi}^{2}] = f_{\text{POD}-2}(\boldsymbol{C}_{p}^{2}) & (\boldsymbol{a}^{2} \in \mathbb{R}^{m_{2} \times r}, \boldsymbol{\Phi}^{2} \in \mathbb{R}^{n_{2} \times m_{2}}) \\
\vdots \\
[\boldsymbol{a}^{k}, \boldsymbol{\Phi}^{k}] = f_{\text{POD}-k}(\boldsymbol{C}_{p}^{k}) & (\boldsymbol{a}^{k} \in \mathbb{R}^{m_{k} \times r}, \boldsymbol{\Phi}^{k} \in \mathbb{R}^{n_{k} \times m_{k}})
\end{cases} (2)$$

where, $0 < m_1, m_2, \cdots, m_k < m$ and $m_1 + m_2 + \cdots + m_k = m$.

Define a comprehensive POD model as $f_{POD} = \{f_{POD-1}, f_{POD-2}, \cdots, f_{POD-k}\}$, equation (2) can be simplified into equation (3).

$$[\mathbf{a}, \mathbf{\Phi}] = f_{\text{POD}}(\mathbf{C}_n) \tag{3}$$

Meanwhile, given a set of installed sensors $x \in \mathbb{R}^{p \times 1}$, the sparse measurements $C_p^S \in \mathbb{R}^{p \times r}$ are obtained by equation (4).

$$C_p^{S} = C_p(x) \tag{4}$$

Furthermore, an RBFNN model (as described in section 3.2) is built to map the sparse measurements C_p ^S to the mode coefficients a, as shown in equation (5).

$$\boldsymbol{a} = f_{\text{RBFNN}}(\boldsymbol{C}_{n}^{S}) \tag{5}$$

So far, the sparse reconstruction model f_{SR} has been built by combing the POD and RBFNN model, which is given by equation (6).

$$\boldsymbol{C}_{n} = f_{SR}(\boldsymbol{C}_{n}^{S}) \tag{6}$$

where, $C_p \stackrel{S}{\longrightarrow} a \stackrel{f_{\text{RBFNN}}}{\longleftarrow} C_p$.

In the reconstructing stage, given the sparse measurements $C_p^{S'} \in \mathbb{R}^{p \times 1}$ under a new flow condition, the mode coefficients $a' \in \mathbb{R}^{m \times 1}$ are first predicted by the RBFNN model, as shown in equation (7).

$$\boldsymbol{a}' = \left[\boldsymbol{a}^{1'}, \boldsymbol{a}^{2'}, \cdots, \boldsymbol{a}^{k'}\right]^{\mathrm{T}} = f_{\mathrm{RBFNN}}\left(\boldsymbol{c}_{p}^{\mathrm{S}'}\right) \tag{7}$$

Then, the surface pressure coefficients $C_p' \in \mathbb{R}^{n \times 1}$ are reconstructed by the POD model f_{POD} , as shown in equation (8).

$$\begin{cases}
\boldsymbol{C}_{p'} = \left[\boldsymbol{C}_{p_{1}}', \boldsymbol{C}_{p_{2}}', \dots, \boldsymbol{C}_{p_{k}}'\right]^{\mathrm{T}} \\
\boldsymbol{C}_{p_{1}}' = f_{\mathrm{POD-1}}'(\boldsymbol{a}^{1'}, \boldsymbol{\Phi}^{1}) \\
\boldsymbol{C}_{p_{2}}' = f_{\mathrm{POD-2}}'(\boldsymbol{a}^{2'}, \boldsymbol{\Phi}^{2}) \\
\vdots \\
\boldsymbol{C}_{p_{k}}' = f_{\mathrm{POD-k}}'(\boldsymbol{a}^{k'}, \boldsymbol{\Phi}^{k})
\end{cases} \tag{8}$$

where, $f_{\text{POD}-i}{}'(i=1,2,\cdots,k)$ represents the POD reconstruction for $f_{\text{POD}-i}$.

2.2 Sensor locations optimization with an enhanced objective function

The sensor locations optimization problem can be expressed as

find
$$\mathbf{x}$$
min $g(\mathbf{x}) = \left| f_{SR} \left(\mathbf{c}_p(\mathbf{x}) \right) - \mathbf{c}_p \right|_1$ (9)

where, $|\cdot|_1$ represents the 1-norm.

Detailed optimization procedure of the sensor locations is shown in Figure 3.

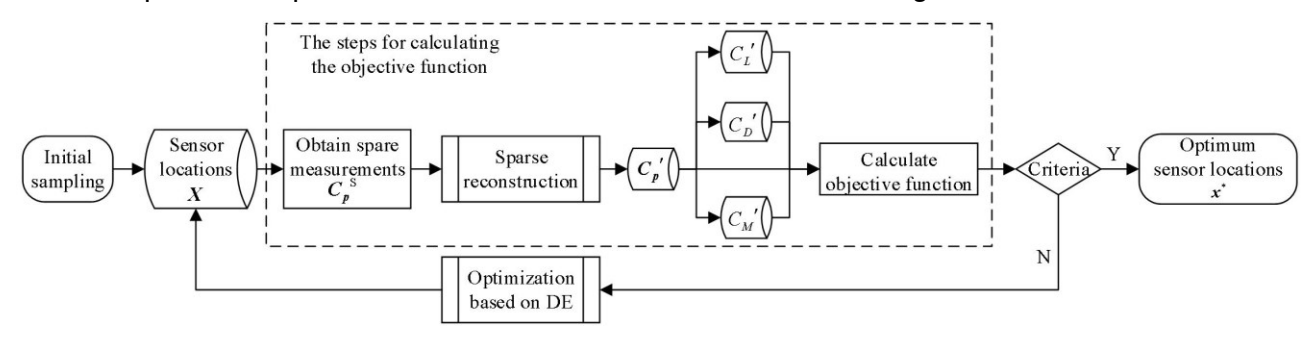


Figure 3 - Flowchart of sensor location optimization with an enhanced objective function

First, an initial set of sensor locations $X \in \mathbb{R}^{p \times N}$ (N represents the population size in optimization) are generated by Latin hypercube sampling (LHS) method.

Then, the steps for solving the objective function are performed. Specifically, $\forall x \in X$, the sparse measurements C_p^S are obtained, and the surface pressure coefficients C_p' are predicted by the sparse reconstruction model. To enhance the sparse reconstruction accuracy, relevant quantities of surface pressure coefficients are introduced into the objective function, including the lift coefficient C_L' , pressure drag coefficient C_D' , and moment coefficient C_M' . These three coefficients are all obtained through the integration of C_p' . Thus, the novel objective function for optimizing the best sensor locations is modified as equation (10).

$$\begin{cases} g = g_0 + \beta \cdot (g_1 + g_2 + g_3) \\ g_0 = \frac{\sum_{i=1}^r |c_{p'i} - c_{pi}|_1}{|max(c_p) - min(c_p)|_1} \\ g_1 = \frac{\sum_{i=1}^r |c_{L'i} - c_{Li}|}{max(c_L) - min(c_L)} \\ g_2 = \frac{\sum_{i=1}^r |c_{D'i} - c_{Di}|}{max(c_D) - min(c_D)} \\ g_3 = \frac{\sum_{i=1}^r |c_{M'i} - c_{Mi}|}{max(c_M) - min(c_M)} \end{cases}$$
(10)

where, g_0 , g_1 , g_2 , and g_4 are normalized objective function for C_p , C_L , C_D , and C_M , respectively; β is the common weight of C_L , C_D , and C_M in objective function.

Subsequently, the population is updated using the DE algorithm, which possesses global optimization capability, and the objective function is reevaluated. Upon meeting the optimization termination criterion, the optimization concludes, and the optimum sensor locations x^* are determined.

The final sparse reconstruction model is expressed as equation (11).

$$\boldsymbol{C}_{p} = f_{SR} \left(\boldsymbol{C}_{p}(\boldsymbol{x}^{*}) \right) \tag{11}$$

3. Basic methods

3.1 Proper orthogonal decomposition

In this work, POD is employed to extract modes from high-dimensional distributed data of various flow properties, such as surface pressure coefficients and surface temperature. The POD modeling process can be described as follows.

A sampled snapshot sequence from flow properties for various conditions by computational fluid dynamics (CFD) simulation is described as $\mathbf{D} = [\mathbf{D}_1, \mathbf{D}_2, \cdots, \mathbf{D}_r]$, where r is the number of sampled conditions, $\mathbf{D}_i (i = 1, 2, \cdots, r)$ is an n-dimensional column vector. Generally, $n \gg r$. We define the mean flow data as $\overline{\mathbf{D}}$, which represents the mean of \mathbf{D}_i and is calculated by equation (12).

$$\bar{\mathbf{D}} = \sum_{i=1}^{r} \mathbf{D}_i / r \tag{12}$$

The standardized flow data $d = [d_1, d_2, \cdots, d_r]$ can be obtained by subtracting \overline{D} from D. To improve computational efficiency, snapshot-POD [21] algorithm is adopted. We define the correlation matrix of d as $C \in \mathbb{R}^{r \times r}$, which is computed by equation (13).

$$C = d^{\mathrm{T}}d \tag{13}$$

Through feature decomposition of ${\bf C}$, the eigenvector matrix ${\bf Q}=[{\bf q}_1,{\bf q}_2,\cdots,{\bf q}_r]\in\mathbb{R}^{r\times r}$ and the eigenvalue matrix ${\bf \lambda}=diag(\lambda_1,\lambda_2,\cdots,\lambda_r)(\lambda_1\geq\lambda_2\geq\cdots\geq\lambda_r)$ are obtained, which satisfies as equation (14).

$$CQ = \lambda Q \tag{14}$$

where ξ_i is POD mode and eigenvalue λ_i represents the energy of ϕ_i ; we define the energy proportion of ξ_i as $k_i = \lambda_i / \sum_{i=1}^r \lambda_i$, which is used to evaluate the contribution of ϕ_i to the flow data. The POD mode matrix $\Phi = [\phi_1, \phi_2, \cdots, \phi_r] \in \mathbb{R}^{n \times r}$ can be computed by equation (15).

$$\phi_i = dq_i / \sqrt{\lambda_i} \tag{15}$$

We define the POD mode coefficients as a, which is calculated as equation (16).

$$\boldsymbol{a} = [\boldsymbol{a}_1, \boldsymbol{a}_2, \cdots, \boldsymbol{a}_r] = \begin{bmatrix} a_1^1 & \cdots & a_r^1 \\ \vdots & \ddots & \vdots \\ a_1^r & \cdots & a_r^r \end{bmatrix} = \boldsymbol{\Phi}^{\mathrm{T}} \boldsymbol{d}$$
 (16)

where $\mathbf{a}_i = \left[a_i^1, a_i^2, \cdots, a_i^r\right]^{\mathrm{T}} (i=1,2,\cdots,r)$ represents the mode coefficient vector corresponding to d. We select the first m modes to build the ROM. Correspondingly, the first m coefficients of \mathbf{a}_i are retained: $\mathbf{a}_i = \left[a_i^1, a_i^2, \cdots, a_i^m\right]^{\mathrm{T}}$. Then, \mathbf{D}_i can be approximately expressed as equation (17).

$$\boldsymbol{D}_{i} \approx \boldsymbol{D}_{i}' = [\boldsymbol{\phi}_{1}, \boldsymbol{\phi}_{2}, \cdots, \boldsymbol{\phi}_{m}] \cdot \boldsymbol{a}_{i} + \overline{\boldsymbol{D}}$$
 (17)

where D_i' is the reconstructed version of the original data D_i .

We define the POD reconstruction error as e, which serves to compare the discrepancy between the original and reconstructed data, assessing the degree of information loss in the POD process. This is calculated as equation (18).

$$e = \frac{1}{r} \sum_{i=1}^{r} \left(\frac{1}{n} \| \mathbf{D}_{i}' - \mathbf{D}_{i} \|_{1} \right)$$
 (18)

where $\|\cdot\|_1$ represents the 1-norm. Generally, specifying the error threshold e_0 allows the value of m to be determined when $e \le e_0$. Besides, the value of m can also be determined by energy proportion analysis [22].

3.2 Radial basis function neural network

RBFNN is widely used in classification and regression due to its simple network structure, strong nonlinear mapping ability and high modeling efficiency. As shown in Figure 4, a typical RBFNN model includes an input layer, a hidden layer, and an output layer. Specifically, the input and output dimension are p and m, respectively. In the hidden layer, the number of neurons is w, and the activation function can be selected from RBFs such as the Gaussian function and the Multiquadric function. The RBFNN model $f_{\rm RBFNN}$ is defined as equation (19).

$$y = f_{\text{RBFNN}}(c) \tag{19}$$

where,
$$\boldsymbol{c} = \begin{bmatrix} c_1, c_2, \cdots, c_p \end{bmatrix}^T$$
, $\boldsymbol{y} = [y_1, y_2, \cdots, y_m]^T$.

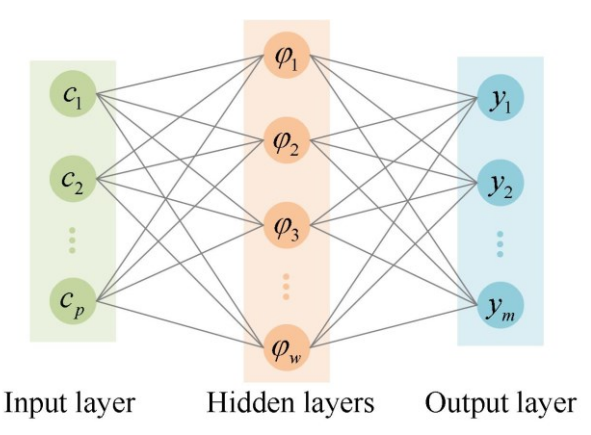


Figure 4 – The architecture of RBFNN

4. Test case

4.1 Description of test case

The proposed method is applied to the *DLR-F6* benchmark geometry, which includes the fuselage, wing, and tail. The surface pressure coefficients are obtained by CFD simulation, and the sparse measurements are extracted from these coefficients. The computational grid is generated using 3-D hybrid mesh. The numbers of the volume meshes and surface meshes are 3.08×10^6 and 1.18×10^5 , respectively.

The flight condition extends for reconstruction modeling are: $Ma \in [0.78, 0.85]$, and $\alpha \in [2^{\circ}, 5^{\circ}]$. Then 300 samples are generated using the random LHS. The density-based compressible Reynolds-averaged Navier-Stokes solver with SST k-omega turbulent model is employed to achieve accurate numerical simulations.

4.2 POD modeling

The dimension of the surface pressure coefficients is 88,210. Based on the characteristics of the aircraft components, the surface pressure coefficients are divided into five groups, illustrated by five different colors in Figure 5. Then, a POD model is established for each group, and the POD reconstruction analysis is performed, resulting in the POD reconstruction errors corresponding to different numbers of modes, as shown in Figure 6. The number of POD modes of each group is determined through POD reconstruction error analysis, with the results presented in Table 1. The results include the recommended range for the number of modes and the number of modes used in this work. The group of wing requires more POD modes due to the strong nonlinear flow properties caused by shock wave [23]. Through POD modeling, the flow characteristics of high-dimensional surface pressure coefficients can be accurately described by 43 mode coefficients.

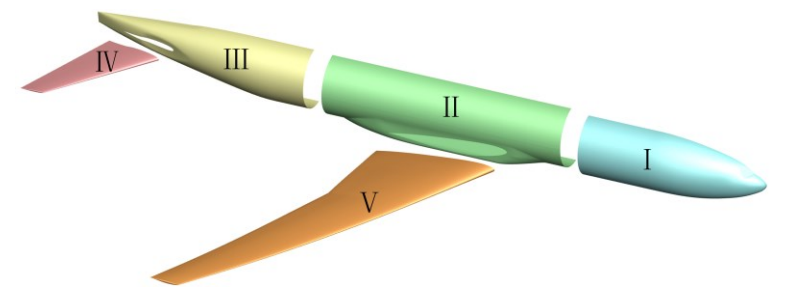


Figure 5 – Five groups based on aircraft components

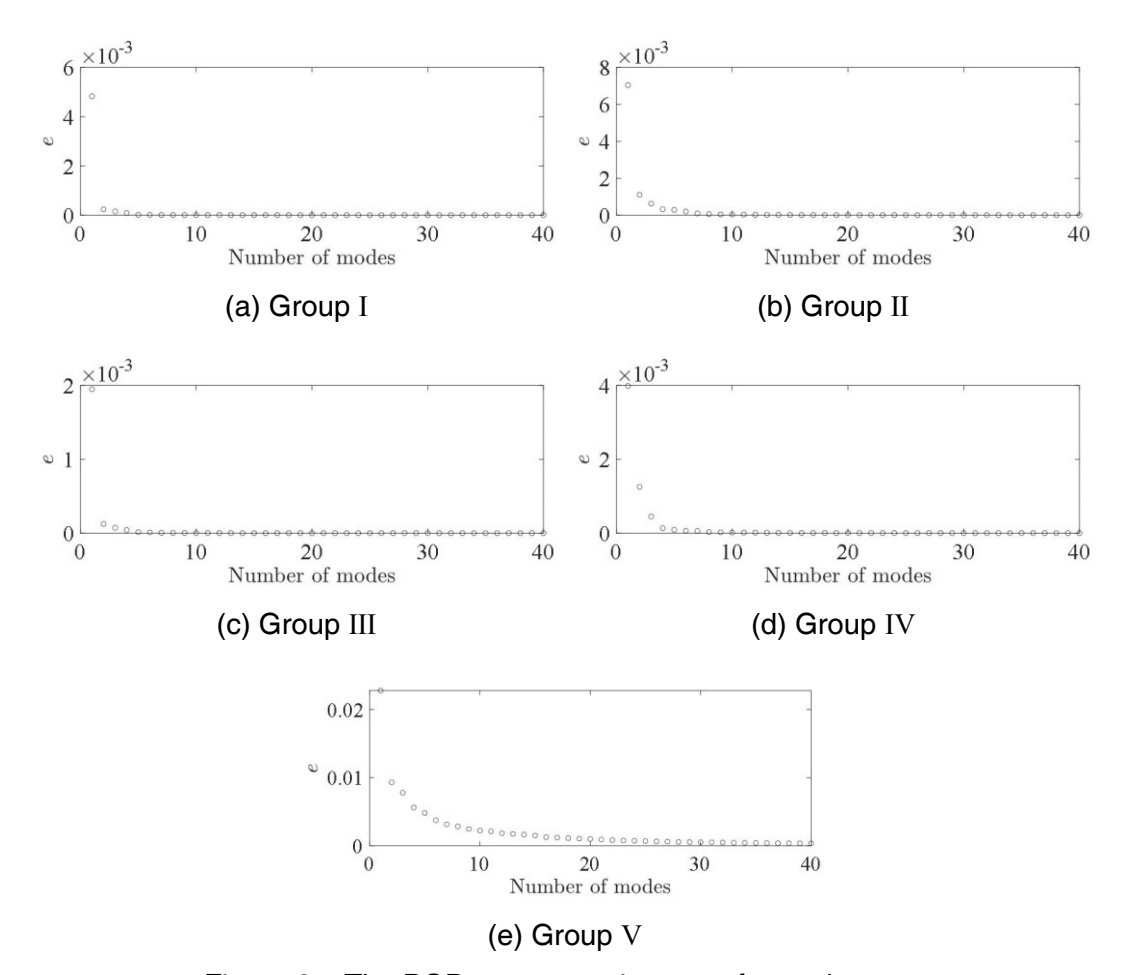


Figure 6 – The POD reconstruction error for each group

Table 1 - The dimension and number of POD modes for each group

Group					
Dimension	8882	11093	8536	20474	39225
Number of POD modes	5(≥ 2)	12(≥ 3)	6(≥ 2)	$10(\ge 4)$	20(≥ 16)

4.3 Parameter analysis

This section introduces parameter analysis about the effect of weight in the objective function and modeling sample size on the accuracy of sparse reconstruction method.

We first analyzed the impact of weight β on the sparse reconstruction accuracy. With the sample size r set to 270, six different weights were set, specifically 0, 0.125, 0.25, 0.5, 1, and 2. Notably, when $\beta=0$, the objective function reduces to considering only surface pressure coefficients. The sparse reconstruction model with different β was repeated modeling 20 times. The reconstructed errors of \mathbf{C}_p under different β are shown in Figure 7. The average value E and variance δ of reconstructed errors are presented in Table 2. For comparison purposes, all results were normalized based on the results with $\beta=0$.

It can be observed that introducing concentrated force coefficients into the objective function affects the reconstruction accuracy of distributed force. When $\beta=0.25$, E and δ for C_p are smaller than those for $\beta=0$, indicating the advantage of the devised objective function. As β increases, the proportion of C_p in the objective function decreases, leading to an upward trend in the reconstruction error of C_p . Therefore, a weight of 0.25 is reasonable for this problem.

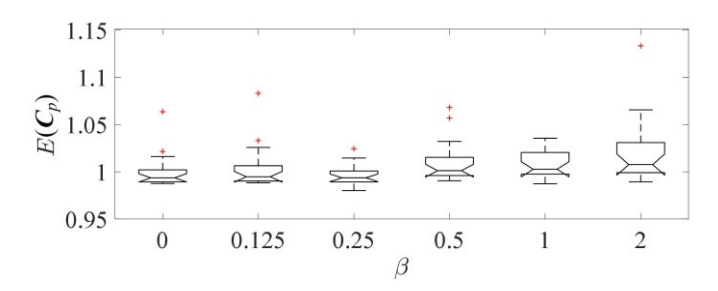


Figure 7 – Reconstruction errors of surface pressure coefficients with different weights

Table 2 - The reconstruction performance with different weights

			•			
Weight	0	0.125	0.25	0.5	1	2
E	1.00	1.0034	0.9967	1.0100	1.0074	1.0206
δ	1.00	1.5842	0.3335	1.4477	0.6958	3.6002

Next, we analyzed the impact of sample size r on model accuracy. With the weight β set to 0.25, the sample sizes were 150, 180, 210, 240, and 270. Each value's corresponding model was trained repeatedly 20 times. The error distribution of C_p is shown in Figure 8. For comparison purposes, all results were normalized based on the results with r=270.

The results indicate that when the sample size decreases to 240, there is no significant change in prediction accuracy. However, as the sample size further decreases, modeling errors gradually increase, and the range of errors expands, suggesting a decrease in both model accuracy and robustness. Therefore, for this problem, a sample size of 240 is deemed reasonable.

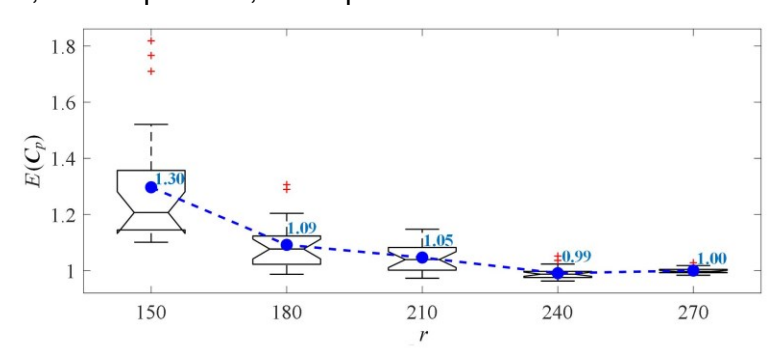


Figure 8 – Variation of sparse reconstruction accuracy with the number of training samples

4.4 Sparse reconstruction results

We use 240 samples for constructing the sparse reconstruction model and 30 samples for performance validation.

In the optimization of sensor locations, the initial number of sensors is set to 50, with each sensor located at the center of a mesh element on the aircraft. Thus, there could be 88,210 possible locations for each sensor. During optimization, if multiple sensors have overlapping locations, only one sensor is retained. The control parameters in optimization are set as: the scaling factor is 0.8, crossover probability is 0.4, the population size is 100, the generation is 200, and the maximum allowed iterations without improvement is 50. Additionally, the weight β in objective function is set to 0.25 based on the analysis results in section 4.3.

The optimum number of sensors is 37, and their distribution is illustrated in Figure 9. The optimized number of sensors in each group is presented in Table 3. It can be seen that the number of sensors for each group is basically consistent with the number of POD modes obtained in Section 4.2, matching the sensor number confirmation theory based on system observability and linear independence [24-25].

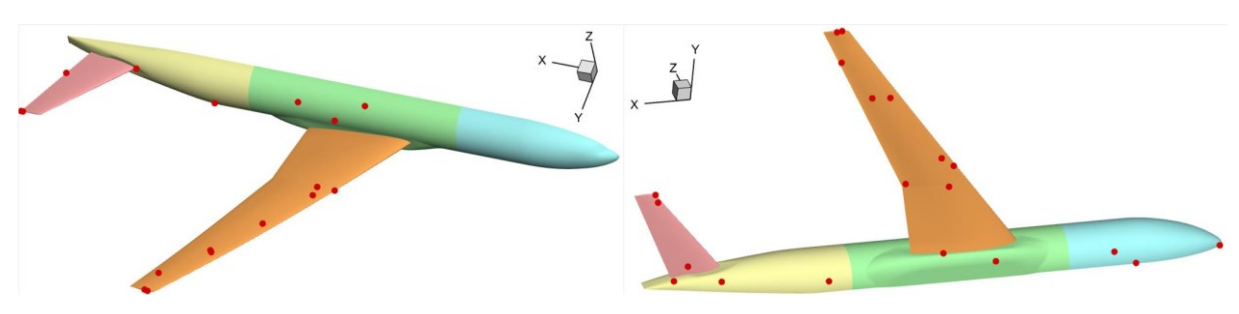


Figure 9 – Optimum sensor locations (red points on the surface)

Figure 9 – Optimum sensor locations (red points on the surface)							
modes and	the optimum	number of	sensors for	each group			
3	5	5	6	18			
		×		x			
	-1.2 -0.8 -0.4 0	0.4 0.8 1.2		-0.02 -0.01 0 0.01 0.02			
z,		x					
		<u> </u>					
(b) Re	constructed	(c)	Reconstruc	tion error			
		` ,					
		*-		×			
	-1.2 -0.9 -0.6 -0.3 0 0.3	0.6 0.9 1.2		-0.04 -0.02 0 0.02 0.04			
	3 (b) Re	modes and the optimum 3 5 (b) Reconstructed ruction results of a test s	modes and the optimum number of 3 5 5 5 5 5 (b) Reconstructed (c)	modes and the optimum number of sensors for 3 5 5 6 (b) Reconstructed (c) Reconstruction results of a test sample ($Ma = 0.7672$, and $Max = 0.7672$), and $Max = 0.7672$.			

(a) Reference (b) Reconstructed (c) Reconstruction error

Figure 11 – Sparse reconstruction results of a test sample (Ma = 0.8338, $\alpha = 4.47^{\circ}$)

The final sparse reconstruction model for surface pressure coefficients can be built based on the optimum sensor number and locations. Figure 10 and Figure 11 illustrate the reconstruction results for two test samples with various flight conditions. It is obvious that the reconstructed surface pressure coefficients agree well with the reference values in most regions, but there are noticeable errors in the central region of the upper surface of the wing. These errors are attributed to the linear assumption in POD [23], resulting in higher POD reconstruction error in the region with shock waves. As the region with large prediction error only occupies a small portion of the entire aircraft surface, the lift, drag, and moment coefficients obtained by integrating the predicted pressure coefficients, have small prediction errors, as shown in Figure 12. The maximum relative error for the lift, drag and moment coefficients are respectively 0.16%, 0.18% and 0.09% of the 30 test samples. The predicted

results above indicate the proposed sparse reconstruction model can reconstruct surface loads on aircraft in good accuracy, with as few sensors as possible.

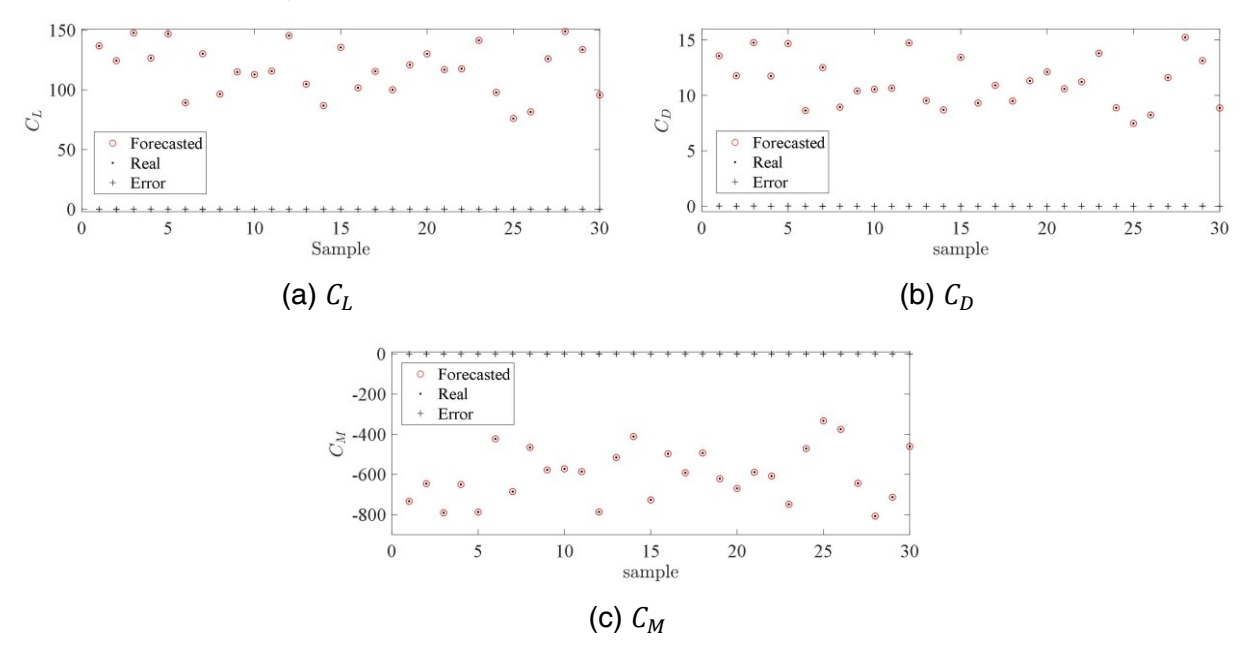


Figure 12 – Predicted results of concentrated forces

5. Conclusion

In this work, a sparse reconstruction model was developed based on POD and RBFNN, and an enhanced objective function by integrating the distributed force. The proposed model was validated by sparse reconstruction of surface pressure coefficients on aircraft *DLR-F6*. The conclusions can be summarized as follows:

- a. For sparse reconstruction problems involving complex shapes, modeling can be performed by partitioning based on component types or aerodynamic data characteristics.
- b. Introducing the integral of surface pressure coefficients into the objective function of sensor optimization and setting appropriate weight can improve the spare reconstruction accuracy of surface pressure coefficients.
- c. Sparse reconstruction errors are mainly concentrated on the upper surface of the wing. This is because this region contains strong nonlinear features, and the POD, based on the linearization assumption in the model, cannot effectively achieve high-precision reconstruction of pressure coefficients.

6. Acknowledgments

This work is funded by the National Natural Science Foundation of China (NSFC Grant No. U2141254).

7. Contact Author Email Address

chunnali@nwpu.edu.cn

8. Copyright Statement

The authors confirm that they, and/or their company or organization, hold copyright on all of the original material included in this paper. The authors also confirm that they have obtained permission, from the copyright holder of any third party material included in this paper, to publish it as part of their paper. The authors confirm that they give permission, or have obtained permission from the copyright holder of this paper, for the publication and distribution of this paper as part of the ICAS proceedings or as individual off-prints from the proceedings.

References

- [1] Zhao X, Deng Z and Zhang W. Sparse reconstruction of surface pressure coefficient based on compressed sensing. *Experiments in Fluids*, Vol. 63, No. 10, p. 156, 2022.
- [2] Huang Y, Zhu C, Xiong W, Wang Y, Jiang Y, Qiu L, Guo D, Hou C, Jiang S, Yang Z, Wang B, Wang L and Yin Z. Flexible smart sensing skin for "Fly-by-Feel" morphing aircraft. *Science China Technological Sciences*, Vol. 65, No. 1, pp 1-29, 2022.
- [3] Voß A and Klimmek T. Parametric aeroelastic modeling, maneuver loads analysis using CFD methods and structural design of a fighter aircraft. *Aerospace Science and Technology*, Vol. 136, p. 108231, 2023.
- [4] Zhao X, Du L, Peng X, Deng Z and Zhang W. Research on refined reconstruction method of airfoil pressure based on compressed sensing. *Theoretical and Applied Mechanics Letters*, Vol. 11, No. 2, p. 100223, 2021.
- [5] Donoho D L. Compressed sensing. *IEEE Transactions on information theory*, Vol. 52, No. 4, pp 1289-1306, 2006.
- [6] Bai Z, Wimalajeewa T, Berger Z, Wang G, Glauser M and Varshney P K. Low-dimensional approach for reconstruction of airfoil data via compressive sensing. *AIAA Journal*, Vol. 53, No. 4, pp 920-933, 2015.
- [7] Sha Y, Xu Y, Yang Q, Wei Y and Wang C. Research on pressure reconstruction of cavitation hydrofoil surface based on compressed sensing. *Ocean Engineering*, Vol. 260, p. 112036, 2022.
- [8] Brunton S L, Noack B R and Koumoutsakos P. Machine learning for fluid mechanics. *Annual review of fluid mechanics*, Vol. 52, pp 477-508, 2020.
- [9] Santos J E, Fox Z R, Mohan A, O'Malley D, Viswanathan H and Lubbers N. Development of the Senseiver for efficient field reconstruction from sparse observations. *Nature Machine Intelligence*, Vol. 5, No. 11, pp 1317-1325, 2023.
- [10]Rowley C W, Dawson S T M. Model reduction for flow analysis and control. *Annual Review of Fluid Mechanics*, Vol. 49, pp 387-417, 2017.
- [11]Zhang X, Ji T, Xie F, Zheng H and Zheng Y. Unsteady flow prediction from sparse measurements by compressed sensing reduced order modeling. *Computer Methods in Applied Mechanics and Engineering*, Vol. 393, p. 114800, 2022.
- [12] Verma S, Papadimitriou C, Lüthen N, Arampatzis G and Koumoutsakos P. Optimal sensor placement for artificial swimmers. *Journal of Fluid Mechanics*, Vol 884, p. A24, 2020.
- [13]Inoba R, Uchida K, Iwasaki Y, Nagata T, Ozawa Y, Saito Y, Nonomura T and Asai K. Optimization of sparse sensor placement for estimation of wind direction and surface pressure distribution using time-averaged pressure-sensitive paint data on automobile model. *Journal of Wind Engineering and Industrial Aerodynamics*, Vol. 227, p. 105043, 2022.
- [14] Jin Y, Wang H, Chugh T, Guo D and Miettinen K. Data-driven evolutionary optimization: An overview and case studies. *IEEE Transactions on Evolutionary Computation*, Vol. 23, No. 3, pp 442-458, 2018.
- [15]Hu Y, Sun Z, Cao L, Zhang Y and Pan P. Optimization configuration of gas path sensors using a hybrid method based on tabu search artificial bee colony and improved genetic algorithm in turbofan engine. *Aerospace Science and Technology*, Vol. 112, p. 106642, 2021.
- [16]Céspedes-Mota A, Castañón G, Martínez-Herrera A F, Cárdenas-Barrón L E and María Sarmiento A. Differential evolution algorithm applied to wireless sensor distribution on different geometric shapes with area and energy optimization. *Journal of Network and Computer Applications*, Vol. 119, pp 14-23, 2018.
- [17] Ferreira B, Antunes A, Carriço N and D Covas. NSGA-II parameterization for the optimal pressure sensor location in water distribution networks. *Urban Water Journal*, Vol. 20, No. 6, pp 738-750, 2023.
- [18]Li J, He S, Martins J R R A, Zhang M and Khoo B C. Efficient data-driven off-design constraint modeling for practical aerodynamic shape optimization. *AIAA Journal*, Vol. 61, No. 7, pp 2854-2866, 2023.
- [19]Ning C and Zhang W. MHA-Net: Multi-source heterogeneous aerodynamic data fusion neural network embedding reduced-dimension features. *Aerospace Science and Technology*, Vol. 145, p. 108908, 2024.
- [20]Sun Z, Wang C, Zheng Y, Bai J, Li Z, Xia Q and Fu Q. Non-intrusive reduced-order model for predicting transonic flow with varying geometries. *Chinese Journal of Aeronautics*, Vol. 33, No. 2, pp 508-519, 2020.
- [21]Wu L, Chen K and Zhan C. Snapshot POD analysis of transient flow in the pilot stage of a jet pipe servo valve. *Journal of Turbulence*, Vol. 19, No. 10, pp 889-909, 2018.
- [22]Jia X, Gong C, Ji W and Li C. Flow sensing method for fluid-structure interaction systems via multilayer proper orthogonal decomposition. *Journal of Fluids and Structures*, Vol. 124, p 104023, 2024.
- [23] Jia X, Li C, Ji W and Gong C. A hybrid reduced-order model combing deep learning for unsteady flow. *Physics of Fluids*, Vol. 34, No. 9, p 097112, 2022.

SPARSE RECONSTRUCTION OF SURFACE LOADS ON AIRCRAFT USING POD AND RBFNN

- [24]Yang C, Liang K and Zhang X. Strategy for sensor number determination and placement optimization with incomplete information based on interval possibility model and clustering avoidance distribution index. *Computer Methods in Applied Mechanics and Engineering*, Vol. 366, p. 113042, 2020.
- [25] An H, Youn B D and Kim H S. A methodology for sensor number and placement optimization for vibration-based damage detection of composite structures under model uncertainty. *Composite Structures*, Vol. 279, p. 114863, 2022.